Letter

Observation of Topological Flat Bands in the Kagome Semiconductor Nb$_3$Cl$_8$

Zhenyu Sun,[∇] Hui Zhou,[∇] Cuixiang Wang,[∇] Shiv Kumar,[∇] Daiyu Geng, Shaosheng Yue, Xin Han, Yuya Haraguchi, Kenya Shimada, Peng Cheng, Lan Chen, Youguo Shi,* Kehui Wu,* Sheng Meng,* and Baojie Feng*

Cite This: https://doi.org/10.1021/acs.nanolett.2c00778

Read Online

ACCESS | Metrics & More | Article Recommendations | SI Supporting Information

ABSTRACT: The destructive interference of wavefunctions in a kagome lattice can give rise to topological flat bands (TFBs) with a highly degenerate state of electrons. Recently, TFBs have been observed in several kagome metals, including Fe$_3$Sn$_2$, FeSn, CoSn, and YMn$_6$Sn$_6$. Nonetheless, kagome materials that are both exfoliable and semiconducting are lacking, which seriously hinders their device applications. Herein, we show that Nb$_3$Cl$_8$, which hosts a breathing kagome lattice, is gapped out because of the absence of inversion symmetry, while the TFBs survive because of the protection of the mirror reflection symmetry. By angle-resolved photoemission spectroscopy measurements and first-principles calculations, we directly observe the TFBs and a moderate band gap in Nb$_3$Cl$_8$. By mechanical exfoliation, we successfully obtain monolayer Nb$_3$Cl$_8$, which is stable under ambient conditions. In addition, our calculations show that monolayer Nb$_3$Cl$_8$ has a magnetic ground state, thus providing opportunities to study the interplay among geometry, topology, and magnetism.

KEYWORDS: breathing kagome lattice, topological flat bands, semiconductor, ARPES, DFT calculations, mechanical exfoliation
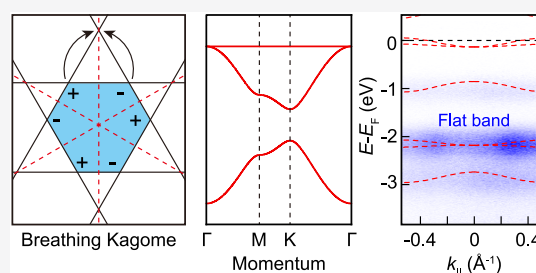
The interplay among geometry, topology, and magnetism at the quantum level can give rise to rich physical properties, and the exploration of novel physics in nontrivial lattices is at the forefront of condensed-matter physics.[1−11] A prototypical example is the kagome lattice, which is composed of corner-sharing triangles (Figure 1a). Such a simple lattice has been intensely studied because of the emergence of topological band structures and frustration-driven spin-liquid states.[12−15] On the basis of a simple s-orbital tight-binding (TB) model with nearest-neighbor hopping, the electronic band structure of the kagome lattice can be described as a Dirac cone capped with a TFB (Figure 1b). The eigenfunctions at neighboring corners have opposite phases, which results in a phase cancellation for hopping to neighboring sites (black arrows in Figure 1a). Therefore, the electronic state is geometrically confined within a single hexagon; this real-space electronic localization leads to a TFB with quenched kinetic energy. The strong electron correlation effects in the highly degenerate flat band can give rise to various exotic properties, including high-temperature superconductivity,[16,17] fractional quantum Hall effects,[14] and Wigner crystal states.[18,19]

Recently, TFBs and Dirac cones have been observed in several kagome metals by angle-resolved photoemission spectroscopy (ARPES), including Fe$_3$Sn$_2$,[1,20] FeSn,[2] CoSn,[3,4] and YMn$_6$Sn$_6$.[5] However, most of the previously discovered kagome materials are metals without a band gap, which means

that the "OFF" state cannot be achieved in devices. This drawback strongly limits their applications in logic and optoelectronic devices.[21,22] Therefore, it is highly desirable to realize semiconducting kagome materials with a moderate band gap, in which the combination of semiconducting properties and TFBs might give rise to exotic physical phenomena, including gate-induced superconductivity[23] and a triplet excitonic insulating state.[24] In addition, the realization of TFBs in semiconductors could enable the tuning of the TFBs by gating or chemical doping. On the other hand, an ideal kagome lattice is only one layer thick, and the non-negligible interlayer coupling in bulk materials will (partially) break the intrinsic properties of the kagome lattice. To date, the experimental realization of layered and exfoliable kagome materials with TFBs is still challenging.

Here, we report a combined experimental and theoretical study on a breathing kagome material, Nb$_3$Cl$_8$. Recently, the existence of TFBs in Nb$_3$Cl$_8$ has been predicted by a high-throughput screening,[11] but experimental investigations of its
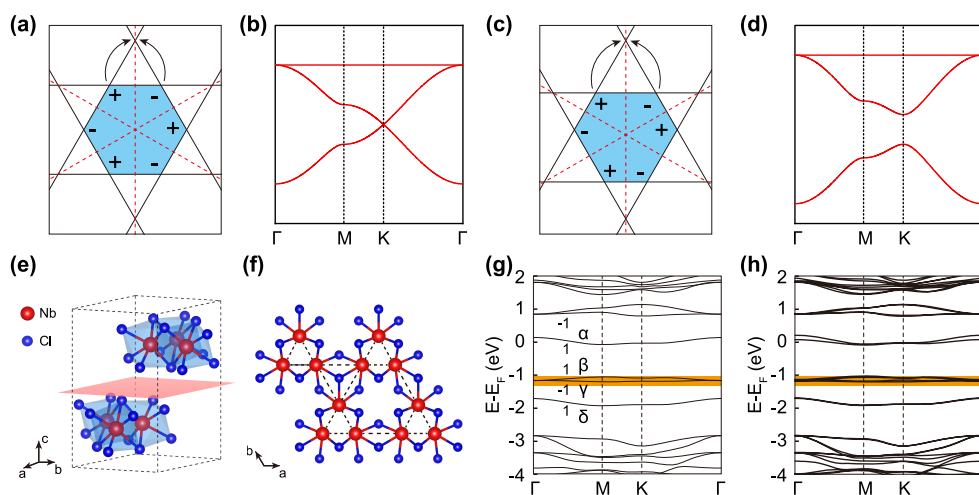
Figure 1. Crystal and electronic structures of the kagome and breathing kagome lattices. (a, c) Schematic drawings of the kagome lattice and breathing kagome lattice, respectively. Electrons are confined in the blue-shaded hexagons because of destructive interference, as indicated by the black arrows. Red dashed lines indicate the mirror axes. (b, d) TB band structure of the kagome lattice and breathing kagome lattice, respectively. The (breathing) kagome lattice has a (gapped) Dirac cone and a topological flat band. (e) Three-dimensional crystal structure of Nb_3Cl_8. Red and blue balls indicate Nb and Cl atoms, respectively. (f) Crystal structure of monolayer Nb_3Cl_8. The Nb atoms form a breathing kagome lattice, as indicated by the black dashed lines. (g, h) Calculated band structures of the monolayer (g) and bulk (h) Nb_3Cl_8 in the paramagnetic state. The parity of the mirror operator along $\Gamma-M$ is labeled by "+" and "−" near each band. The four bands that have been observed by ARPES measurements are indicated by α, β, γ, and δ, respectively.
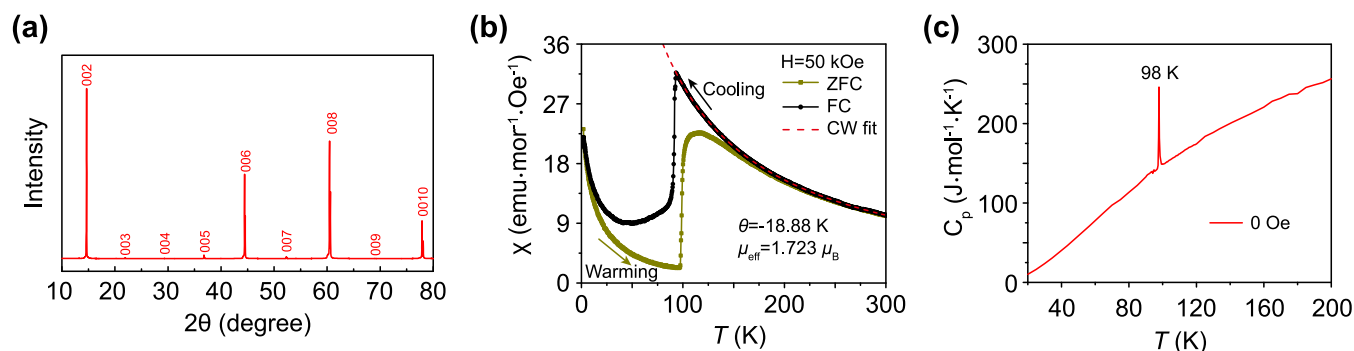

Figure 2. Characterization of the basic physical properties of Nb_3Cl_8. (a) X-ray diffraction pattern of the Nb_3Cl_8 single crystal. (b) Temperature dependence of the magnetic susceptibility (χ) of Nb_3Cl_8. The red dashed line indicates the fitting results using the Curie–Weiss function. (c) Temperature dependence of the heat capacity of Nb_3Cl_8.

electronic structure are still lacking. Our ARPES and optical absorption spectroscopy measurements confirmed the existence of TFBs and a moderate band gap (~1.12 eV). By mechanical exfoliation, we successfully obtained monolayer Nb_3Cl_8, a key step for device applications. In addition, Nb_3Cl_8 is expected to have a magnetic ground state, which implies the existence of exotic properties arising from the interplay between magnetism and band topology.

First, we briefly discuss the band structure of the breathing kagome lattice (Figure 1c) on the basis of a TB model. The degeneracy of the Dirac point in the conventional kagome lattice is protected by inversion symmetry. In the breathing kagome lattice, however, the absence of inversion symmetry will gap out the Dirac cone, leading to a semiconducting ground state, as shown in Figure 1d. On the other hand, destructive phase interference, the key reason for the emergence of TFBs, is protected by three equivalent mirror axes (red dashed lines in Figure 1a,c). These mirror symmetries survive in the breathing kagome lattice, and thus, the breathing kagome lattice still hosts TFBs. A detailed TB analysis is presented in the Supporting Information.

Next, we study the van der Waals material Nb_3Cl_8, which has a breathing kagome lattice in each layer.[25−29] Bulk Nb_3Cl_8 crystallizes in a layered structure with a space group of $P\overline{3}m1$ (Figure 1e). Within each layer, the Nb atoms form a breathing kagome lattice, as shown in Figure 1f. The calculated band structure of monolayer Nb_3Cl_8 is displayed in Figure 1g. One can directly see a flat band at approximately 1.1 eV below the Fermi level, which has the narrowest bandwidth, as highlighted by the orange region. In addition, our orbital and symmetry analysis has confirmed the phase-destructive interfering behavior of this band, which is the key character of kagome TFBs (see the Supporting Information for details). The Dirac cones are gapped out, resulting in multiple gaps. Notably, the α band crosses the Fermi level, indicating a metallic ground state. However, we will show later that the ground state should be semiconducting because DFT calculations underestimate the gap, as confirmed by our ARPES and optical absorption spectroscopy measurements. Because of the weak interlayer van der Waals interaction, the band structure of bulk Nb_3Cl_8 is analogous to that of monolayer Nb_3Cl_8, as shown in Figure 1h.
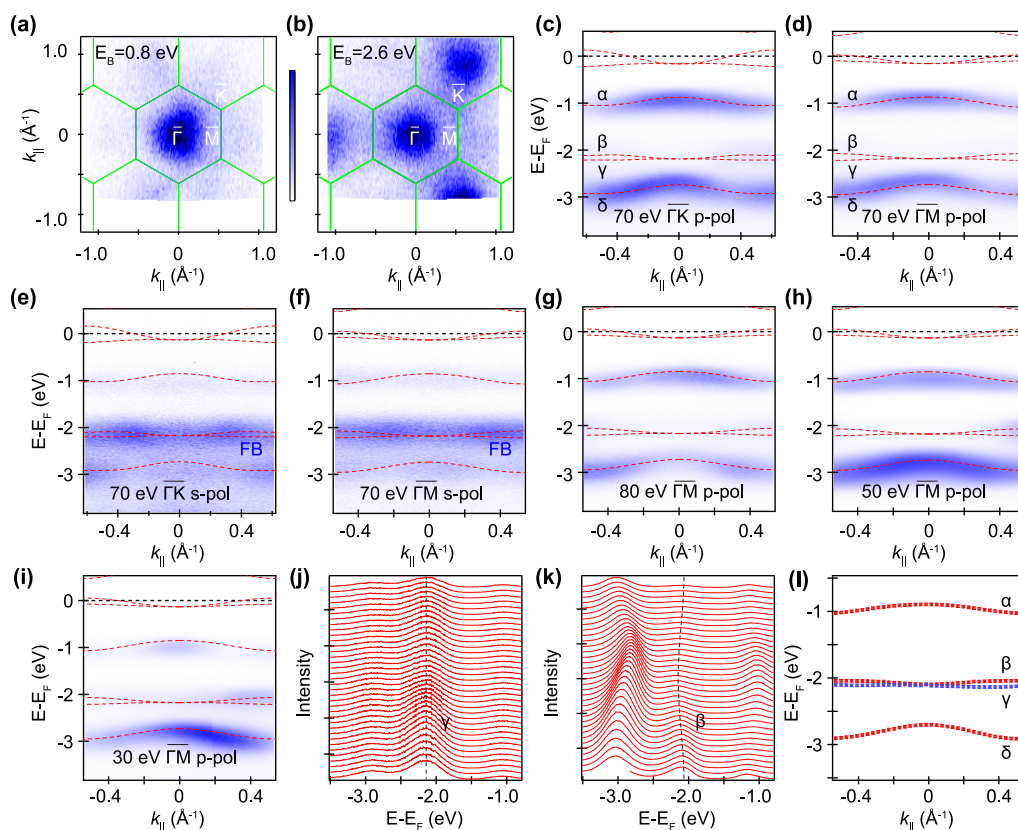
Figure 3. ARPES measurements of Nb_3Cl_8. (a, b) Constant energy contours at $E_B = 0.8$ and 2.6 eV, respectively. Green lines indicate the BZs of monolayer Nb_3Cl_8. (c–i) ARPES intensity plots along the $\overline{\Gamma}-\overline{K}$ and $\overline{\Gamma}-\overline{M}$ directions with different photon energies and polarizations. The calculated band structures of monolayer Nb_3Cl_8 are superimposed on each panel after shifting the Fermi level 0.8 eV toward a higher binding energy. (j, k) Energy distribution curves of (f) and (i), respectively. Black dashed lines indicate the γ and β bands, respectively. (l) Fitted dispersions of the four bands based on the peaks in energy distribution curves. The α and δ bands are fitted using the data in (c), the γ band is fitted using the data in (f), and the β band is fitted using the data in (h).

As a result, the TFBs survive in bulk Nb_3Cl_8, which is favorable for ARPES measurements.

High-quality Nb_3Cl_8 single crystals were synthesized by the flux method (see Methods). Figure 2a shows an XRD spectrum measured along the (00l) direction, and only the 00l peaks were observed. The sharp peaks indicate the high quality of the crystals. The temperature-dependent magnetic susceptibility of Nb_3Cl_8 is displayed in Figure 2b. As the temperature decreases, the magnetic susceptibility of Nb_3Cl_8 drops abruptly at ∼100 K with a prominent hysteresis. Above 100 K, the temperature dependence of the magnetic susceptibility can be well fitted by the Curie–Weiss function, as indicated by the red dashed line in Figure 2b, and the fitted Θ value is −18.88 K. The negative Θ value indicates an antiferromagnetic ground state. These results agree well with previous works.[26] In addition, the heat capacity shows a sharp λ-shaped peak at approximately ∼98 K (Figure 2c), in line with the transition temperature determined from the magnetic susceptibility measurements. This phase transition was interpreted as a slight change in layer stacking, which does not affect the structure within each layer.[26] Therefore, the topological properties of Nb_3Cl_8 are also not affected by the phase transition.

We then performed ARPES measurements to confirm the TFBs in Nb_3Cl_8. Because of the semiconducting nature of Nb_3Cl_8, there is no detectable photoemission signal at the Fermi level. With increasing binding energies, we observe strong spectral weight near the Γ point of the first Brillouin

zone (BZ) from $E_B \approx 0.8$ eV, as shown in Figure 3a. The spectral weight in the second BZ is much weaker because of the photoemission matrix element effect. The constant energy contour at $E_B \approx 2.6$ eV shows clear hexagonal symmetry (Figure 3b), in agreement with the crystal structure of Nb_3Cl_8. The band structures along the $\overline{\Gamma}-\overline{K}$ and $\overline{\Gamma}-\overline{M}$ directions are displayed in Figure 3c–i. A careful comparison with the calculation results shows that the chemical potential has an ∼0.8 eV shift toward higher binding energies. After the chemical potential is readjusted, the calculated band structures agree well with our ARPES results except for a slight discrepancy at the Fermi level, as indicated by the red dashed lines. The discrepancy at the Fermi level will be discussed later. Within 3.5 eV of the Fermi level, we observed four prominent bands: α, β, γ, and δ. Notably, the TFB, i.e. the γ band, can be observed in the whole BZ and has negligible dispersion, as shown in Figure 3e,f,j. The β band, which is very close to the γ band, has a stronger spectral weight with low photon energies (Figure 3i). In contrast with the flat band, the β band disperses with momentum, as shown in Figure 3k. Figure 3l shows the fitted dispersions of the four bands, which agree well with our calculation results.

During ARPES measurements, we find that the spectral weight of each band varies with the polarization of the incident light: the α, β, and δ bands are more sensitive to p-polarized light, while the γ band is more sensitive to s-polarized light, despite the intensity variation with photon energy. To understand this phenomenon, we focus on the bands along

$\overline{\Gamma}-\overline{M}$ because $\overline{\Gamma}-\overline{M}$ is a mirror axis and each band along this direction has definite odd or even parity when spin−orbit coupling is neglected. The calculation results are indicated by "+" (even) and "−" (odd) in Figure 1g. We find that the α, β, and δ bands have even parity, which can only be observed by p-polarized light. The γ band, i.e. the flat band, has odd parity and can only be detected by s-polarized light. These analyses agree well with our ARPES results, which further confirms the existence of TFBs in Nb_3Cl_8. Neglecting the variation in relative intensity, we find that all bands have negligible dispersion with photon energy (or k_z), in agreement with the two-dimensional nature of Nb_3Cl_8.

Next, we discuss the discrepancy near the Fermi level between the experimental and calculation results: the calculation results show the existence of bands after adjusting the chemical potential, while we did not observe any bands in our ARPES measurements. A possible reason for this discrepancy is the underestimation of the band gap in DFT calculations.[30] On the basis of our ARPES results, the valence band maximum is located at ~0.9 eV below the Fermi level, which indicates that the actual band gap is larger than 0.9 eV. To determine the band gap of Nb_3Cl_8, we performed optical absorption spectroscopy measurements. Figure 4a shows a typical absorption spectrum of Nb_3Cl_8, and several absorption peaks are observed from the ultraviolet to near-infrared regions. There is one prominent peak at 1.12 eV, which can be assigned to the transition from valence to conduction bands, as indicated by the blue arrow in Figure 4b. Therefore, the optical band gap is ~1.12 eV, which is approximately 0.23 eV larger than the calculation results. It should be noted that there is a broader peak centered at ~6250 cm^{-1} (0.775 eV). This feature is within the band gap and might originate from defects or edge states.[31,32] Since the valence band maximum is located at $E_B \approx 0.9$ eV, the conduction band bottom is expected to be located at >0.22 eV above the Fermi level, which is not accessible in our ARPES measurements.

Thus far, we have demonstrated that Nb_3Cl_8 hosts TFBs because of the breathing kagome lattice. Strictly speaking, however, a kagome lattice refers to a monolayer material; the non-negligible interlayer coupling in bulk materials could be detrimental to the intrinsic properties of the kagome lattice. Therefore, it is highly desirable to obtain monolayer kagome materials for their applications in quantum devices. Because of the weak van der Waals interaction in bulk Nb_3Cl_8, ultrathin flakes can be easily obtained by mechanical exfoliation.[27] Figure 4c shows a typical optical microscope image of an ultrathin Nb_3Cl_8 flake, and Figure 4d shows an atomic force microscope (AFM) image in the white box of Figure 4c. The height of the thinnest flake is approximately 0.8 nm with respect to the substrate (Figure 4e), which is comparable to the lattice constant of bulk Nb_3Cl_8 in the perpendicular direction (~0.61 nm). The quality of ultrathin Nb_3Cl_8 was also confirmed by Raman spectroscopy measurements, as shown in Figure 4f. Most of the Raman peaks of the bulk Nb_3Cl_8 survive in the monolayer limit with a negligible shift. It should be noted that our AFM and Raman spectroscopy measurements were performed under ambient conditions, and the strong intensity of Raman peaks indicates the high stability of monolayer Nb_3Cl_8 in air. Stability in air is an essential prerequisite for potential device applications.

To summarize, we provide compelling evidence for the existence of TFBs in Nb_3Cl_8, which has a breathing kagome lattice. The semiconducting nature of Nb_3Cl_8 provides
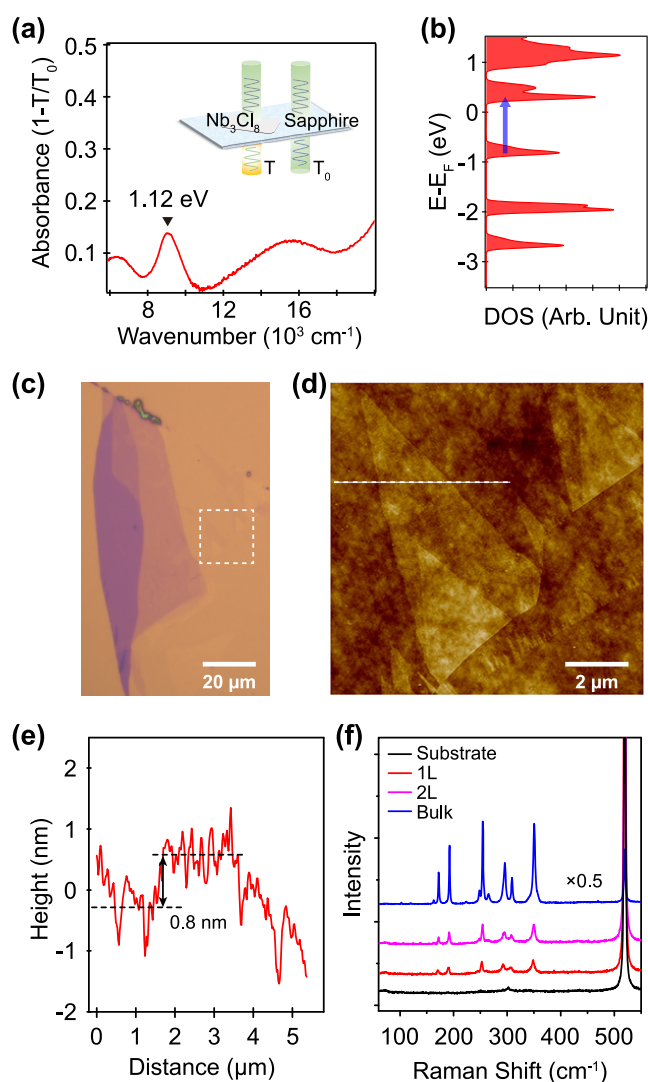

Figure 4. Optical absorption measurements and mechanical exfoliation of Nb_3Cl_8. (a) Extinction spectrum $(1 - T/T_0)$ of a 20 nm thick Nb_3Cl_8 flake. The supporting substrate is sapphire. (b) Calculated local density of states. The chemical potential and band gap were adjusted according to our experimental results. The blue arrow indicates the optical transition from the valence band maximum to the conduction band minimum. (c) Optical microscope image of an exfoliated Nb_3Cl_8 flake. (d) AFM image in the white box in (c). (e) Line profile along the white dashed line in (d). (f) Raman spectra of 1L, 2L, and bulk Nb_3Cl_8.

opportunities to fabricate optoelectronic and logic devices. Few- and single-layer Nb_3Cl_8 can be easily obtained by mechanical exfoliation and are quite stable under ambient conditions, which is an essential prerequisite for their device applications. In addition, our calculations show that the ground state of monolayer Nb_3Cl_8 is ferromagnetic and the TFBs will spin-split because of the magnetic exchange interaction (see the Supporting Information). In contrast with conventional and nonmagnetic kagome lattices, the breaking of symmetries in breathing kagome lattices, including inversion and time reversal, can give rise to multiple topological states, such as higher-order topological insulators/semimetals,[33−35] Chern insulators,[36] and chiral charge densities.[17]

■ METHODS

Single crystals of Nb_3Cl_8 were grown using $PbCl_2$ as a flux. High-purity Nb (Alfa Aesar 99.99%) and $NbCl_5$ (Alfa Aesar 99.9%) were mixed in a molar ratio of 7:8 and placed in an alumina crucible. The crucible was sealed in a quartz tube under vacuum, heated at 750 °C for 150 h, and cooled to room temperature naturally. The excess $PbCl_2$ flux was removed by sonicating in hot water. ARPES measurements were performed at Beamline BL-1 of the Hiroshima Synchrotron Radiation Center.[37] Clean surfaces required for the ARPES measurements were obtained by cleaving the samples *in situ* in an ultrahigh-vacuum chamber. Both the cleavage and the measurements were performed at room temperature to avoid charging effects. Nb_3Cl_8 thin flakes can be exfoliated on various substrates, including SiO_2/Si, $Au/SiO_2/Si$, and sapphire, using blue Nitto tapes. Freshly cleaved surfaces were attached to the precleaned substrates, followed by carefully peeling off the tape. Thin flakes that contain few- to monolayer Nb_3Cl_8 remained on the substrates. The thicknesses and morphologies of Nb_3Cl_8 flakes were examined by AFM (Oxford, Asylum Research Cypher S) in tapping mode. Raman spectra were collected using a confocal Raman system (Horiba LanRam HR Evolution) with 532 nm laser excitation. Optical absorption measurements were carried out using a commercial spectrometer (MStarter ABS, Metatest Corporation).

First-principles calculations based on density functional theory were performed with the Vienna *ab initio* simulation package.[38,39] The projector-augmented wave pseudopotential[40] and Perdew−Burke−Ernzerhof exchange-correlation functional[41] were used. The energy cutoff of the plane-wave basis was set at 350 eV. For monolayer Nb_3Cl_8, the vacuum space was set to be larger than 15 Å. The first BZ was sampled according to the Γ-centered scheme. For monolayer (bulk) Nb_3Cl_8, we used a k mesh of $6 \times 6 \times 1$ ($6 \times 6 \times 6$) for structural optimization and $12 \times 12 \times 1$ ($9 \times 9 \times 9$) for the self-consistent calculations. The positions of the atoms were optimized until the convergence of the force on each atom was less than 0.01 eV/Å. The convergence condition of the electronic self-consistent loop was 10^{-5} eV.

■ ASSOCIATED CONTENT

ⓢ Supporting Information

The Supporting Information is available free of charge at https://pubs.acs.org/doi/10.1021/acs.nanolett.2c00778.

> Generalizing the destructive phase interference to a breathing kagome lattice, inversion symmetry breaking induced gap opening in the kagome lattice, determination of the magnetic ground state of monolayer Nb_3Cl_8, topological properties of the flat bands in Nb_3Cl_8, orbital and symmetry analysis of the flat band (PDF)

■ AUTHOR INFORMATION

Corresponding Authors

Youguo Shi − *Institute of Physics, Chinese Academy of Sciences, Beijing 100190, People's Republic of China; School of Physical Sciences and Center of Materials Science and Optoelectronics Engineering, University of Chinese Academy of Sciences, Beijing 100049, People's Republic of China; Songshan Lake Materials Laboratory, Dongguan, Guangdong 523808, People's Republic of China;* Email: ygshi@iphy.ac.cn

Kehui Wu − *Institute of Physics, Chinese Academy of Sciences, Beijing 100190, People's Republic of China; School of Physical Sciences, University of Chinese Academy of Sciences, Beijing 100049, People's Republic of China; Songshan Lake Materials Laboratory, Dongguan, Guangdong 523808, People's Republic of China;* orcid.org/0000-0002-7698-5673; Email: khwu@iphy.ac.cn

Sheng Meng − *Institute of Physics, Chinese Academy of Sciences, Beijing 100190, People's Republic of China; School of Physical Sciences, University of Chinese Academy of Sciences, Beijing 100049, People's Republic of China;* orcid.org/0000-0002-1553-1432; Email: smeng@iphy.ac.cn

Baojie Feng − *Institute of Physics, Chinese Academy of Sciences, Beijing 100190, People's Republic of China; School of Physical Sciences, University of Chinese Academy of Sciences, Beijing 100049, People's Republic of China;* orcid.org/0000-0003-2332-7949; Email: bjfeng@iphy.ac.cn

Authors

Zhenyu Sun − *Institute of Physics, Chinese Academy of Sciences, Beijing 100190, People's Republic of China; School of Physical Sciences, University of Chinese Academy of Sciences, Beijing 100049, People's Republic of China*

Hui Zhou − *Institute of Physics, Chinese Academy of Sciences, Beijing 100190, People's Republic of China; School of Physical Sciences, University of Chinese Academy of Sciences, Beijing 100049, People's Republic of China*

Cuixiang Wang − *Institute of Physics, Chinese Academy of Sciences, Beijing 100190, People's Republic of China; School of Physical Sciences, University of Chinese Academy of Sciences, Beijing 100049, People's Republic of China*

Shiv Kumar − *Hiroshima Synchrotron Radiation Center, Hiroshima University, Higashi-Hiroshima 739-0046, Japan*

Daiyu Geng − *Institute of Physics, Chinese Academy of Sciences, Beijing 100190, People's Republic of China; School of Physical Sciences, University of Chinese Academy of Sciences, Beijing 100049, People's Republic of China*

Shaosheng Yue − *Institute of Physics, Chinese Academy of Sciences, Beijing 100190, People's Republic of China; School of Physical Sciences, University of Chinese Academy of Sciences, Beijing 100049, People's Republic of China;* orcid.org/0000-0002-5111-7562

Xin Han − *Institute of Physics, Chinese Academy of Sciences, Beijing 100190, People's Republic of China; School of Physical Sciences, University of Chinese Academy of Sciences, Beijing 100049, People's Republic of China*

Yuya Haraguchi − *Department of Applied Physics and Chemical Engineering, Tokyo University of Agriculture and Technology, Tokyo 184-8588, Japan;* orcid.org/0000-0002-6951-5112

Kenya Shimada − *Hiroshima Synchrotron Radiation Center, Hiroshima University, Higashi-Hiroshima 739-0046, Japan;* orcid.org/0000-0002-1945-2352

Peng Cheng − *Institute of Physics, Chinese Academy of Sciences, Beijing 100190, People's Republic of China; School of Physical Sciences, University of Chinese Academy of Sciences, Beijing 100049, People's Republic of China;* orcid.org/0000-0001-5963-1390

Lan Chen − *Institute of Physics, Chinese Academy of Sciences, Beijing 100190, People's Republic of China; School of Physical Sciences, University of Chinese Academy of Sciences,*

Beijing 100049, People's Republic of China; Songshan Lake Materials Laboratory, Dongguan, Guangdong 523808, People's Republic of China; ⓞ orcid.org/0000-0003-4426-9944

Author Contributions

▽Z.S., H.Z., C.W., and S.K. contributed equally to this work. B.F. conceived the research. C.W., X.H., Y.H., and Y.S. synthesized the crystals. Z.S., S.K., D.G., S.Y., and B.F. performed the ARPES measurements. Z.S. exfoliated the sample and performed optical absorption spectroscopy and AFM measurements. H.Z. and S.M. performed theoretical calculations and analysis. All authors contributed to the discussion of the data and writing of the manuscript.

Notes

The authors declare no competing financial interest.

■ ACKNOWLEDGMENTS

■ REFERENCES

(1) Lin, Z.; Choi, J.-H.; Zhang, Q.; Qin, W.; Yi, S.; Wang, P.; et al. Flatbands and emergent ferromagnetic ordering in Fe_3Sn_2 kagome lattices. *Phys. Rev. Lett.* **2018**, *121*, 096401.

(2) Kang, M.; Ye, L.; Fang, S.; You, J.-S.; Levitan, A.; Han, M.; et al. Dirac fermions and flat bands in the ideal kagome metal FeSn. *Nat. Mater.* **2020**, *19*, 163−169.

(3) Kang, M.; Fang, S.; Ye, L.; Po, H. C.; Denlinger, J.; Jozwiak, C.; Bostwick, A.; Rotenberg, E.; Kaxiras, E.; Checkelsky, J. G.; Comin, R. Topological flat bands in frustrated kagome lattice CoSn. *Nat. Commun.* **2020**, *11*, 4004.

(4) Liu, Z.; Li, M.; Wang, Q.; Wang, G.; Wen, C.; Jiang, K.; Lu, X.; Yan, S.; Huang, Y.; Shen, D.; Yin, J.-X.; Wang, Z.; Yin, Z.; Lei, H.; Wang, S. Orbital-selective Dirac fermions and extremely flat bands in frustrated kagome-lattice metal CoSn. *Nat. Commun.* **2020**, *11*, 4002.

(5) Li, M.; Wang, Q.; Wang, G.; Yuan, Z.; Song, W.; Lou, R.; Liu, Z.; Huang, Y.; Liu, Z.; Lei, H.; Yin, Z.; Wang, S. Dirac cone, flat band and saddle point in kagome magnet YMn_6Sn_6. *Nat. Commun.* **2021**, *12*, 3129.

(6) Weeks, C.; Franz, M. Topological insulators on the Lieb and perovskite lattices. *Phys. Rev. B* **2010**, *82*, 085310.

(7) Sun, K.; Gu, Z.; Katsura, H.; Sarma, S. D. Nearly flatbands with nontrivial topology. *Phys. Rev. Lett.* **2011**, *106*, 236803.

(8) Slot, M. R.; Gardenier, T. S.; Jacobse, P. H.; van Miert, G. C. P.; Kempkes, S. N.; Zevenhuizen, S. J. M.; Smith, C. M.; Vanmaekelbergh, D.; Swart, I. Experimental realization and characterization of an electronic Lieb lattice. *Nat. Phys.* **2017**, *13*, 672−676.

(9) Kempkes, S. N.; Slot, M. R.; van den Broeke, J. J.; Capiod, P.; Benalcazar, W. A.; Vanmaekelbergh, D.; Bercioux, D.; Swart, I.; Smith, C. M. Robust zero-energy modes in an electronic higher-order topological insulator. *Nat. Mater.* **2019**, *18*, 1292−1297.

(10) Yin, J.; Ma, W.; Cochran, T. A.; Xu, X.; Zhang, S. S.; Tien, H. J.; et al. Quantum-limit Chern topological magnetism in $TbMn_6Sn_6$. *Nature* **2020**, *583*, 533−536.

(11) Liu, H.; Meng, S.; Liu, F. Screening two-dimensional materials with topological flat bands. *Phys. Rev. Mater.* **2021**, *5*, 084203.

(12) Guo, H.-M.; Franz, M. Topological insulator on the kagome lattice. *Phys. Rev. B* **2009**, *80*, 113102.

(13) Balents, L. Spin liquids in frustrated magnets. *Nature* **2010**, *464*, 199−208.

(14) Tang, E.; Mei, J.-W.; Wen, X.-G. High-temperature fractional quantum Hall states. *Phys. Rev. Lett.* **2011**, *106*, 236802.

(15) Han, T.-H.; Helton, J. S.; Chu, S.; Nocera, D. G.; Rodriguez-Rivera, J. A.; Broholm, C.; Lee, Y. S. Fractionalized excitations in the spin-liquid state of a kagome lattice antiferromagnet. *Nature* **2012**, *492*, 406−410.

(16) Imada, M.; Kohno, M. Superconductivity from flat dispersion designed in doped Mott insulators. *Phys. Rev. lett.* **2000**, *84*, 143.

(17) Jiang, Y.-X.; Yin, J.-X.; Denner, M. M.; Shumiya, N.; Ortiz, B. R.; Xu, G.; et al. Unconventional chiral charge order in kagome superconductor KV_3Sb_5. *Nat. Mater.* **2021**, *20*, 1353−1357.

(18) Jiang, H.-C.; Devereaux, T.; Kivelson, S. A. Holon Wigner crystal in a lightly doped kagome quantum spin liquid. *Phys. Rev. Lett.* **2017**, *119*, 067002.

(19) Jaworowski, B.; Güçlü, A. D. G.; Kaczmarkiewicz, P.; Kupczyński, M.; Potasz, P.; Wójs, A. Wigner crystallization in topological flat bands. *New J. Phys.* **2018**, *20*, 063023.

(20) Ye, L.; Kang, M.; Liu, J.; von Cube, F.; Wicker, C. R.; Suzuki, T.; Jozwiak, C.; Bostwick, A.; Rotenberg, E.; Bell, D. C.; Fu, L.; Comin, R.; Checkelsky, J. G. Massive Dirac fermions in a ferromagnetic kagome metal. *Nature* **2018**, *555*, 638−642.

(21) Liu, Y.; Weiss, N. O.; Duan, X.; Cheng, H.-C.; Huang, Y.; Duan, X. Van der Waals heterostructures and devices. *Nat. Rev. Mater.* **2016**, *1*, 16042.

(22) Liu, C.; Chen, H.; Wang, S.; Liu, Q.; Jiang, Y.-G.; Zhang, D. W.; Liu, M.; Zhou, P. Two-dimensional materials for next-generation computing technologies. *Nat. Nanotechnol.* **2020**, *15*, 545−557.

(23) Ye, J. T.; Zhang, Y. J.; Akashi, R.; Bahramy, M. S.; Arita, R.; Iwasa, Y. Superconducting dome in a gate-tuned band insulator. *Science* **2012**, *338*, 1193−1196.

(24) Sethi, G.; Zhou, Y.; Zhu, L.; Yang, L.; Liu, F. Flat-band-enabled triplet excitonic insulator in a diatomic kagome lattice. *Phys. Rev. Lett.* **2021**, *126*, 196403.

(25) Miller, G. J. Solid state chemistry of Nb_3Cl_8: Nb_3TeCl_7, mixed crystal formation, and intercalation. *J. Alloys Compd.* **1995**, *217*, 5−12.

(26) Haraguchi, Y.; Michioka, C.; Ishikawa, M.; Nakano, Y.; Yamochi, H.; Ueda, H.; Yoshimura, K. Magnetic-nonmagnetic phase transition with interlayer charge disproportionation of Nb_3 trimers in the cluster compound Nb_3Cl_8. *Inorg. Chem.* **2017**, *56*, 3483−3488.

(27) Yoon, J.; Lesne, E.; Sklarek, K.; Sheckelton, J.; Pasco, C.; Parkin, S. S. P.; McQueen, T. M.; Ali, M. N. Anomalous thickness-dependent electrical conductivity in van der Waals layered transition metal halide, Nb_3Cl_8. *J. Phys.: Condens. Matter* **2020**, *32*, 304004.

(28) Pasco, C. M.; El Baggari, I.; Bianco, E.; Kourkoutis, L. F.; McQueen, T. M. Tunable magnetic transition to a singlet ground state in a 2D van der Waals layered trimerized kagome magnet. *ACS Nano* **2019**, *13*, 9457−9463.

(29) Sheckelton, J. P.; Plumb, K. W.; Trump, B. A.; Broholmbcd, C. L.; McQueen, T. M. Rearrangement of van der Waals stacking and formation of a singlet state at T = 90 K in a cluster magnet. *Inorg. Chem. Front.* **2017**, *4*, 481−490.

(30) Perdew, J. P.; Yang, W.; Burke, K.; Yang, Z.; Gross, E. K. U.; Scheffler, M.; Scuseria, G. E.; Henderson, T. M.; Zhang, I. Y.; Ruzsinszky, A.; Peng, H.; Sun, J.; Trushin, E.; Görling, A. Understanding band gaps of solids in generalized Kohn-Sham theory. *Proc. Natl. Acad. Sci. U. S. A.* **2017**, *114*, 2801−2806.

(31) Roxlo, C. B.; Daage, M.; Rupper, A. F.; Chianelli, R. R. Optical absorption and catalytic activity of molybdenum sulfide edge surfaces. *J. Catal.* **1986**, *100*, 176−184.

(32) Chen, J.; Wang, J.; Yu, Q.; Wang, T.; Zhang, Y.; Chen, C.; Li, C.; Wang, Z.; Zhu, S.; Ding, X.; Wang, L.; Wu, J.; Zhang, K.; Zhou, P.; Jiang, Z. Sub-band gap absorption and optical nonlinear response of $MnPSe_3$ nanosheets for pulse generation in the L-band. *ACS Appl. Mater. Interfaces* **2021**, *13*, 13524−13533.

(33) Bolens, A.; Nagaosa, N. Topological states on the breathing kagome lattice. *Phys. Rev. B* **2019**, *99*, 165141.

(34) Wakao, H.; Yoshida, T.; Araki, H.; Mizoguchi, T.; Hatsugai, Y. Higher-order topological phases in a spring-mass model on a breathing kagome lattice. *Phys. Rev. B* **2020**, *101*, 094107.

(35) Ezawa, M. Higher-order topological insulators and semimetals on the breathing kagome and pyrochlore lattices. *Phys. Rev. Lett.* **2018**, *120*, 026801.

(36) Ren, Y.; Jiang, H.-C.; Qiao, Z.; Sheng, D. Orbital chern insulator and quantum phase diagram of a kagome electron system with half-filled flat bands. *Phys. Rev. Lett.* **2021**, *126*, 117602.
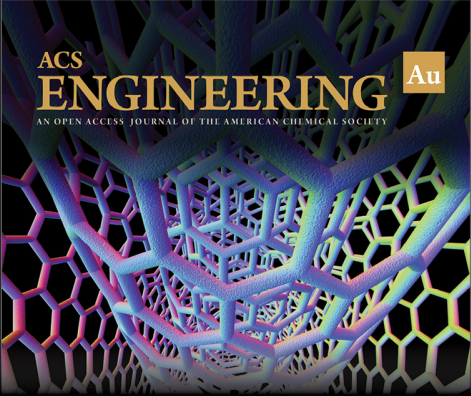
(37) Iwasawa, H.; Shimada, K.; Schwier, E. F.; Zheng, M.; Kojima, Y.; Hayashi, H.; Jiang, J.; Higashiguchi, M.; Aiura, Y.; Namatame, H.; Taniguchi, M. Rotatable high-resolution ARPES system for tunable linear-polarization geometry. *J. Synchrotron Radiat.* **2017**, *24*, 836−841.

(38) Kresse, G.; Hafner, J. Ab initio molecular dynamics for liquid metals. *Phys. Rev. B* **1993**, *47*, 558.

(39) Kresse, G.; Furthmüller, J. Efficient iterative schemes for ab initio total-energy calculations using a plane-wave basis set. *Phys. Rev. B* **1996**, *54*, 11169−11186.

(40) Blöchl, P. E. Projector augmented-wave method. *Phys. Rev. B* **1994**, *50*, 17953−17979.

(41) Perdew, J. P.; Burke, K.; Ernzerhof, M. Generalized gradient approximation made simple. *Phys. Rev. Lett.* **1996**, *77*, 3865.